geotechnics

MDPI

Article

Geological Exploration, Landslide Characterization and Susceptibility Mapping at the Boundary between Two Crystalline Bodies in Jajarkot, Nepal

Yubraj Bikram Shahi [1], Sushma Kadel [1], Harish Dangi [2,*], Ganesh Adhikari [3], Diwakar KC [2,†] and Kabi Raj Paudyal [1]

[1] Central Department of Geology, Tribhuvan University, Kirtipur, Kathmandu 44618, Nepal
[2] NEA Engineering Company Limited, Trade Tower, Thapathali, Kathmandu 44600, Nepal
[3] Department of Geology, Tri-Chandra Multiple Campus, Tribhuvan University, Kathmandu 44605, Nepal
* Correspondence: harishhappy27@gmail.com
† Present address: Department of Civil and Environmental Engineering, University of Toledo, Toledo, OH 43606, USA.

Abstract: The geology of the Himalayas is intricated and intriguing. It features numerous tectonic bodies and structures too complex to interpret. Along with such mysteries it has too many common geohazards, such as landslides. In this study, a detailed geological investigation is carried out to overcome the discrepancies in structural interpretation, the nature of two crystalline bodies, and non-uniformity in geological mapping in the central Himalayan arc, in the Jajarkot district of Nepal. Along with the geological exploration and landslide characterization of the area, consequent landslide susceptibility mapping is performed considering 13 causative factors related to geology, topography, land use, hydrology, and the anthropogenic factor, using two bivariate statistical models. This study concludes that the two metamorphic crystalline bodies in the study area are most probably the klippen, due to the absence or erosion of the root zone. The field study revealed that haphazard road excavation without the consideration of geological and geotechnical features has caused shallow landslides. The results obtained from the susceptibility maps, with a varying range of susceptibility zones, are in good agreement with the spatial distribution of pre-historic landslides. The results of the susceptibility modeling are validated by calculating landslide density and plotting area under curves (AUC). The AUC value for the WOE, and the FR method, revealed an overall success rate of 79.42% and 77.62%, respectively.

Keywords: landslides; debris flows; hazard; susceptibility; frequency ratio; weight of evidence

check for updates

Citation: Shahi, Y.B.; Kadel, S.; Dangi, H.; Adhikari, G.; KC, D.; Paudyal, K.R. Geological Exploration, Landslide Characterization and Susceptibility Mapping at the Boundary between Two Crystalline Bodies in Jajarkot, Nepal. *Geotechnics* **2022**, 2, 1059–1083. https://doi.org/10.3390/geotechnics2040050

Academic Editors: Daniel Dias, Qi Wang, Bei Jiang, Xuezhen Wu and Hongke Gao

Received: 18 October 2022
Accepted: 25 November 2022
Published: 1 December 2022

1. Introduction

The Himalayan Orogeny is the perfect example of continent-continent collision that occurred obliquely at around 65 Ma [1], when the Indian plate moved towards the Eurasian plate. This collision was later followed by anticlockwise rotation of the Indian plate and collision around 50 Ma [2]. The conversion velocity of the Indian plate and Eurasian plate decreased significantly from 15 to 4 cm/year at about 50–35 Ma [3]. Still, the Indian plate is moving towards the north and is pushing the Eurasian plate with a movement speed of 2 cm/year, making the youngest mountain range tectonically still active [4,5], and making the area vulnerable to geohazards.

Geo-hazards such as landslides, debris flows, glacier lake outburst flood (GLOF), mudflows, earthquake and earthquake-triggered landslides, and debris flows are common in the fragile Himalayas [6]. The growing population and development of road networks, infrastructures, settlements, and lifelines have increased the frequency and impact of natural hazards, especially landslides and debris flows [7]. Worldwide, between the years 1994 and 2013, 218 million people were affected by natural disasters annually [8]. Among all the natural hazards, landslides and debris flows are the most frequent and are responsible for the destruction of lives, property, and natural settings. Landslides and debris flow account for 17% of all deaths caused by natural hazards [9]. Landslides are caused by factors such as incompetent lithological and geological conditions, rugged topography and relief, and are triggered by natural agents such as rainfall [10,11] and anthropogenic actions such as land use pattern [12]. Landslides are sometimes triggered by the movement of active faults and earthquakes [13]. Debris flows are often mobilized from shallow landslides [14,15] and later converted into extreme flows with the addition of water and the entrainment of solid mass along the downslope.

Landslides and debris flows are most frequent within the region of active tectonism with distinctive geological structures and differential lithostratigraphy. The lesser Himalayan region in the Himalayan arc has suffered from multiple events of mass movements because of fragile geology and high-intensity rainfall [16–19]. The topography around the Chheda Khola watershed in the Jajarkot district, Nepal, has been continuously hit by various events of mass movements. Such events have impacted the area with socio-economic losses; to mitigate the impact, potential landslide-prone areas should be identified [20]. A landslide susceptibility map indicates where future landslides are likely to occur by identifying the areas of previous landslide occurrences, and areas with similar or identical physical characteristics [21,22]. It divides a spatial area into zones of varying likelihoods of landslide occurrence [23]. The investigation of landslide contributing factors, and the selection of an effective approach, are critical for the preparation of a landslide susceptibility map. In the area of active tectonics, the identification of the detailed lithological units, precise geological structure placement, along with the preparation of the accurate landslide inventory, play a vital role in such mapping.

The Lesser Himalaya, also known as thrust-and-fold belt, has complex geological settings due to the folding and thrusting of crystalline sequences. The western and the central part of the Nepal Himalaya comprises numerous crystalline bodies, which are core of great Himalayan syncline or anticline. Among well-known crystalline in Nepal Himalaya, two metamorphic cryatalline bodies i.e., Jajarkot Crystalline Zone and Karnali Crystalline Zone, are located along the study area [24–26]. The Jajarkot Crystalline Zone consists of sheared phyllite, schists, and blasto-mylonitic augen gneiss [25]. The Karnali Crystalline Zone consists of kyanite sillimanite–bearing gneiss, calc-silicate gneiss, migmatitic gneiss, and augen gneiss [27]. Some of the researchers have intrepreted them as klippen, while some others have interpreted them as nappes [25–27]. Although many researchers have worked on the study area, this region still lacks uniform geological and structural interpretation. One of the major interests of this study is to investigate whether the crystalline bodies present in the study area are klippen or nappes. Further, there are no studies carried out on landslide characterization and landslide susceptibility assessment. To address these issues the following studies are carried out:

- A detailed geological exploration is carried out to generate the precise geological map of the study area.
- A field survey on landslide occurrence patterns is carried out.
- The geological and geo-structural control on landslide occurrence are investigated.
- Landslide susceptibility modeling is conducted using two bivariate statistical approaches, Frequency Ratio (FR) and Weight of Evidence (WOE), to explore and predict the probability distribution of future landslides in the area.

2. Study Area

The study area lies in the southern part of Jajarkot district, Karnali Province, Mid-Western Nepal, between latitude and longitude of 28.677557 N, 82.053348 E, and 28.838401 N, 82.110773 E, covering an area of approximately 190 km^2 (Figure 1). It is about 600 km west of Kathmandu, Nepal's capital, and is accessible by regular air services from Kathmandu to Birendranagar in Surkhet and Nepalgunj in Banke district. From both of these airstrips, there is a well-paved road leading up to Chheda, which is in the southern part of the study area, and a fairweather gravel road connects Chheda with Thalaha. Yet, most of the study areas are hardly accessible due to uneven topography, difficult terrain, and a lack of infrastructure.

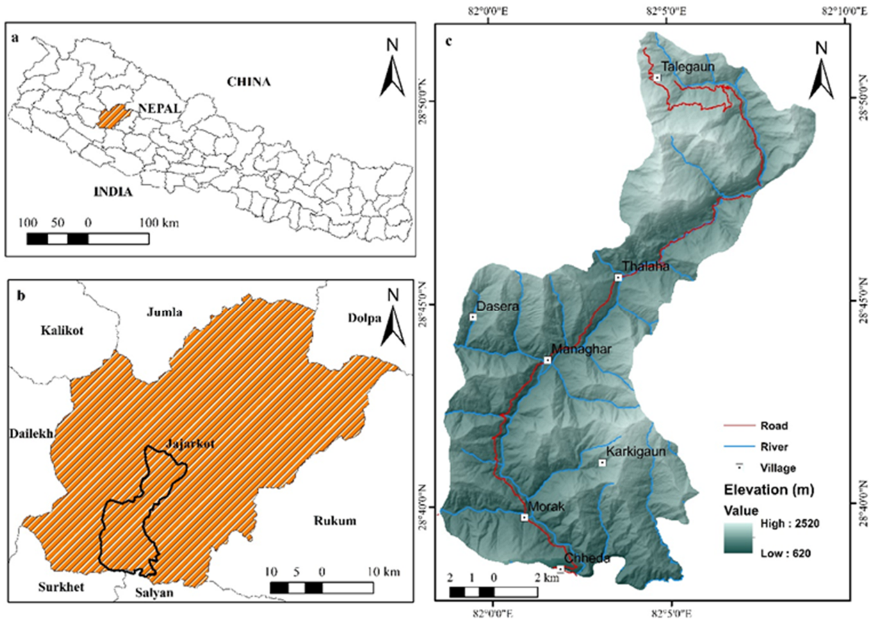

Figure 1. Location map of the study area: (**a**) Jajarkot district in Nepal around neighboring countries; (**b**) location of the study area within Jajarkot district and bordering districts of Nepal; (**c**) the study area with major streams.

The geomorphology of the study area is characterized by highly elevated mountains, extremely rugged topography, and river valleys with uneven relief. Peak, saddle, spur, ridge, valley, river valley, alluvial terrace, and frequent colluvial cones are the common geomorphic features. The topography of the area is highly dissected and rough with elevations ranging from 620 m to 2520 m. Geologically the study area lies in the Lesser Himalayan Crystalline zone consisting of sheared phyllite, schists, blasto-mylonitic, augen gneiss, kyanite-sillimanite–bearing gneiss, calc-silicate gneiss, migmatitic gneiss, and augen gneiss [28,29].

3. Methodology

Initially, a preliminary landslide inventory map was prepared using topographic maps and high-resolution Google Earth images. After that, fieldwork was conducted for detailed geological investigation via multiple routes. Systematic sample collection, in situ permeability testing, landslide characterization, and a validation of the preliminary landslide inventory map was carried out during the field investigation. The collected rock samples were further tested in the lab.

In this study, 13 causative factors were considered for landslide susceptibility mapping. Along with the field investigation of the geology and landslides, the required data for the investigation on causative factors of the landslide was collected from several sources. Furthermore, landslide susceptibility modeling was performed using two bivariate statistical methods: the Weight of Evidence (WOE) and the Frequency Ratio (FR). The results of these two methods were verified by calculating the landslide density and plotting the success rate curve.

3.1. Data Acquisition and Data Processing

The investigation on the causes of past landslides can be used as the source for predicting future landslides [30]. For this, it is necessary to prepare and analyze the landslide contributing factors. The Digital Elevation Model (DEM) of raster format 20 m × 20 m, prepared using the contour data provided by Department of Survey (DOS) [31] has been used to prepare some data base of the predisposing factors (slope, aspect, SPI, TWI). Based on the DEM, topography factors, slope gradient, slope aspect, slope shape, TWI, SPI, and hydrological factors including river and stream proximity data, were derived. Rainfall intensity in the study area was analyzed using the data obtained from the Department of Hydrology and Meteorology (DHM) [32]. Land use map and distances to road map were prepared using digital data from the DOS. Maps related to geology and tectonism were developed from field investigation. All these data layers were transferred into 20 m × 20 m pixel size raster format. The data processing was carried out using GIS.

3.2. Landslide Susceptibility Modeling

Landslide susceptibility modeling can be grouped into four categories: landslide inventories, heuristic, statistical and deterministic approaches, among which statistical methods have been widely applied. Likewise, this study applies two well-known bivariate statistical methods; the WOE and the FR. The WOE method is a quantitative method used to combine datasets used for various purposes [33–35]. In this method, weights for each landslide conditioning factor are calculated based on the presence or absence of landslides within the different classes of a causative factor [33,34]. The equations involved are given in Equations (1) and (2):

$$W^{+} = \ln \frac{P\{F|L\}}{P\{F|\overline{L}\}} \tag{1}$$

$$W^{-} = \ln \frac{P\{\overline{F}|L\}}{P\{\overline{F}|\overline{L}\}} \tag{2}$$

where W^{+} = weight for the presence of landslides, W^{-} = weight absence of landslides within a certain class of causative factor map. $P\ (F/L)$ = conditional probability of F occurring given the presence of L, a bar above a symbol signifies the negation.

The weights can be calculated easily by cross tabulating the observed landslide map with the causative factor map using Equations (3) and (4).

$$W^{+} = \ln \frac{N\{F \cap L\}/N\{L\}}{N\left\{F \cap \overline{L}\right\}/N\{\overline{L}\}} \tag{3}$$

$$W^{-} = \ln \frac{N\{\overline{F} \cap L\}/N\{L\}}{N\left\{\overline{F} \cap \overline{L}\right\}/N\{\overline{L}\}} \tag{4}$$

$C = W^{+} - W^{-}$ is a contrast and gives the probability of occurrence of landslides for the particular area after combining all the conditioning factors. C is positive for the positive correlation and negative for non-correlation.

The frequency ratio is the ratio of the probability of an occurrence to the probability of a non-occurrence of landslides for any given set of attributes [36]. The lower the value of the frequency ratio, the weaker the correlation. The value of the frequency ratio can be estimated by using the approach followed by KC et al. [37]. The equation used is given in Equation (5).

$$FR = \ln \frac{L_c}{A_c} \tag{5}$$

where L_c is percentage of in particular class; is calculated as:

$$L_c = \mathrm{N\ (A\,|\,L)/N\ (L)} \times 100\%,$$

where N (A | L) = the number of landslide pixels within class A. N (L) = the total number of landslide pixels in the map.

Ac is the percentage of the specific class A of the entire study area; it can be calculated as:

$$\mathrm{A_c} = \mathrm{N\ (A)/N_t} \times 100\%,$$

where N (A) = the number of pixels of a specific class. N_t = the total number of pixels of the entire study area on the map.

4. Results

Results can briefly be grouped into two categories: preparation of a new geological map accompanied by detailed geological investigation; and landslide characterization and landslide susceptibility mapping.

4.1. Geology

Based on lithological characteristics, stratigraphic setup, tectonic and structural features, and a consideration of the regional geological picture, three tectonic units have been recognized in the study area: Jajarkot Klippe, Lesser Himalaya, and Karnali Klippe. Although there is not uniformity in using the terms nappe and klippe for these two cryatalline bodies, the term klippe has been used here following the work of Dhital [35]. These three tectonic units consist of an unmetamorphosed to incipiently metamorphosed rock sequence that runs from south to north, with a layer of unmetamorphosed Lesser Himalayan rock sequence between two thrust sheets (Figure 2). Not only do the three units have distinct lithological characteristics, but they also have distinct metamorphic gradation and deformation.

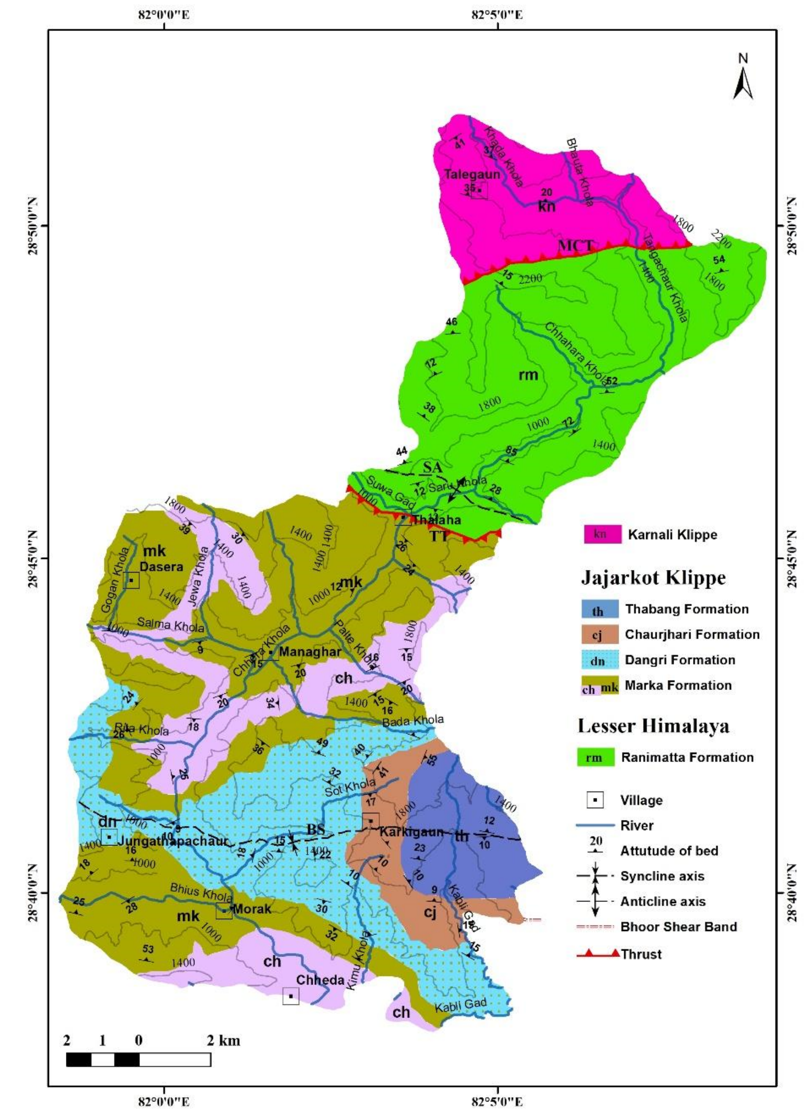

Figure 2. Geological map of the study area representing the region between Chhedachaur to Saureni.

4.1.1. Lithostratigraphy

The Karnali Klippe, assumed to be the eastern end of the Almora-Dadeldhura nappe in Western Nepal [38], is composed of high-grade metamorphic rocks resembling the rocks of the Higher Himalaya. It consists of tourmaline-bearing granitic augen gneisses, coarsely crystalline quartz gneisses, and kyanite-bearing banded gneisses, with garnetiferous schist in the south. The upper Karnali Klippe is composed of coarsely crystalline granitic augen gneiss intercalated with kyanite grade paragneiss with frequent pegmatitic intrusions, while the lower portion consists of kyanite-garnet gneiss, coarsely crystalline quartz-gneiss, and coarsely crystalline quartzites.

Despite the fact that Hagen [39] introduced the term “Jajarkot Nappe”, the current observation concludes that it is klippe. The four-rock formation of Jajarkot Klippe has well-established rock succession within the limits of their tectonic boundaries (Figure 2). They are Marka Formation, Dangri Formation, Chaurjhari Formation, and Thabang Formation, representing older to the younger sequence stratigraphically.

The Marka Formation [40] is comprised mainly of light grey to pale yellow micaceous quartzites with intercalations of blue-grey garnet schists. In the upper part of this formation, near the Thalaha Thrust (Figure 2), basic intrusion and graphitic schist intercalations are more common. The Marka Formation also contains a mappable meta-diamictite succession, the Chhera Diamictite, which has been mapped as a member due to constraint in lateral continuity of the succession. The lower contact of the Chhera Diamictite [40] is rather sharp, but the contact in the Bheri River section appears to be indistinct and truncated; this is inferred as disconformity [40], while the upper contact is transitional. This rock succession is made up of thin-to-medium bedded, gray, crenulated, calcareous meta-diamictite with angular to sub-rounded clasts of gray dolomite, gray gneiss, schists, and pale yellow and pink quartzite metamorphosed to garnet grade. The proportion of clast in meta-diamictite ranges from 1% to 12% and is strongly stretched parallel to foliation.

The Dangri Formation [41] consists of crenulated, grey, and grey-green garnetiferous schists and mica schists that alternate with very thick-bedded, medium to coarse-grained, laminated grey, yellow, and white quartzites. Both psammitic and pelitic schists predominate over quartzites (about 70%); the quartzite-schist transition is gradational. Intercalation of the gritty layer (psammitic schist) and pelitic schists gives rise to the gneissic appearance in this region.

The Chaurjhari Formation [42] is composed of medium-grained, coarsely crystalline muscovite-biotite-quartz schists, crenulated garnetiferous schists, and graphitic schists with light grey micaceous quartzite; the density and size of the garnet have increased in this formation. Garnet porphyroblasts in schists reach up to 4 mm in diameter.

The Thabang Formation [42] unit’s rocks are well represented by thinly to thickly bedded coarsely crystalline white, bluish grey to purple limestone marbles interbedded with garnetiferous mica schists, forming the core of the syncline (Figure 2).

The Lesser Himalayan meta-sediments between these two nappes consist of only one rock unit, the Ranimatta Formation, which is named after the village Ranimatta by Dhital [40] and has been retained for similar rock successions in the study area. The lower part of the Ranimatta Formation is composed of parallel laminated, infrequently ripple marked fine-to-medium grained pale grey, yellow, or white quartzite with medium to coarse-grained meta-basic intrusions. The upper part contains a gray to green-gray phyllitic meta-sandstone succession that is occasionally intercalated with quartzites.

4.1.2. Structures

Within the study area, there are four megascopic structures: the south-dipping Thalaha Thrust (TT), the gently north-dipping Main Central Thrust (MCT), and two large-scale gently plunging, non-cylindrical syncline and anticline fold, Suwa Gad Anticline (SA) and Bhoor Syncline (BS) (Figure 2). The Thalaha Thrust, named after the village Thalaha in the present study, is equivalent to the Mahabharat Thrust (MT) [43] of the Kathmandu Nappe and the Dubung Thrust of the Kahun Klippe [44]. The MCT overrides the Lesser

Himalayan rocks and places it over the high-grade metamorphic rocks of the Higher Himalayan crystalline slab. The TT, on the other hand, juxtaposed the Lesser Himalayan meta-sedimentary sequence (footwall) with the Lesser Himalayan crystalline sequence as the Jajarkot Nappe rocks (hanging wall).

These structural discontinuities are delineated based on the presence of outcrop-scaled deformation structures such as parasitic folds trending N–S, crenulations trending E–W, and brittle shear zones, as well as microstructures and attitudes of the beds. Meso and microstructural observations, as well as measurements of asymmetrical boudins, projection of lineation data, and axis measurement of small parasitic folds, revealed top-to-the-south movement throughout the area, indicating southward propagation of the TT and the MCT. Figure 3 shows two structural features exhibiting top-to-the-south movement. Furthermore, multiple shear zones form the linear pattern along the eastern part of the area, from which a shear band is delineated (Figure 2).

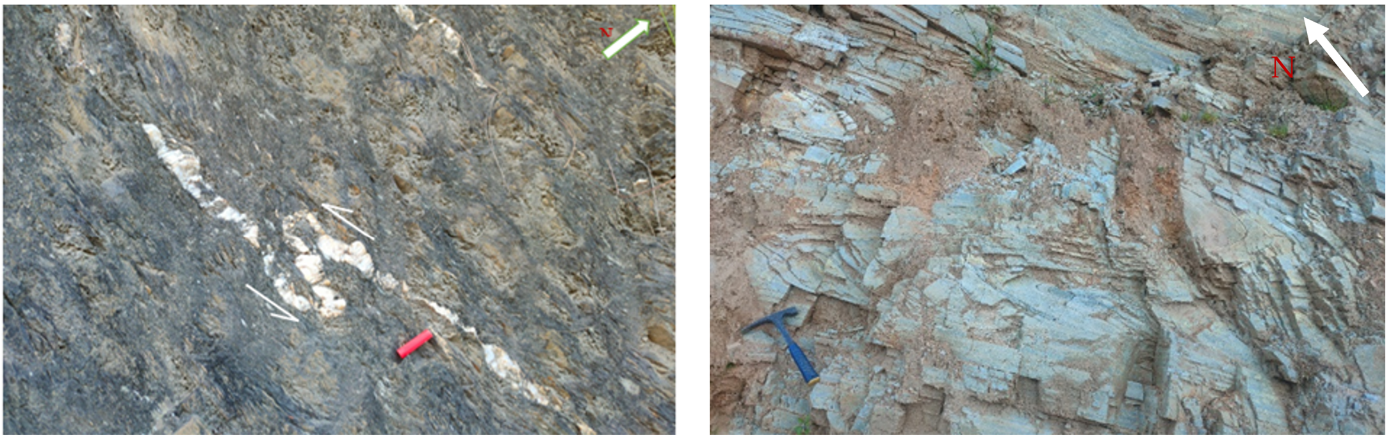

(**a**) (**b**)

Figure 3. Meso-scale geological structures showing top-to-the-south movement: (**a**) S-type folded vein exposed in Dasera section; (**b**) Z-type drag fold exposed in Karkigaun section.

4.2. Landslide Occurrence Pattern and Landslide Inventory

The study area is dominated by excavation-induced shallow landslides (Figure 4), with the volume of failure surface ranging from 20 cubic meters to 38,000 cubic meters covering the area from 25 square meters to 7600 square meters. Several deep-seated complex paleo-landslides with volumes exceeding 1000 cubic meters which were shoveling settlements, agricultural lands, and even human life (Figure 4) were discovered. Failures occurred primarily along colluvium, residual soil, and bedrock, with very few landslides occurring at soil-bedrock contacts. Approximately 50% of landslides are initiated in bedrock, while residual soils, colluvium, and soil-bedrock contact account for around 18%, 29%, and 3% of total landslides, respectively. The landslide deposition materials are dominated by coarse gravels (Figure 4), with coarse and fine deposits covering around 89.5% and 10.5% of the total landslide deposits, respectively. According to the USCS soil classification scheme, soil categories GP, GM, and GC account for approximately 63%, 4%, and 23% of total deposits, respectively, while fine soils ML and CL account for 5% of total deposits. In the study area, the translational type of failure appeared to be the most prevalent. Because of the entrainment of water on its way toward the downslope, most of the landslides have converted into debris flows.

Figure 4. Some photographic references of the landslides reported within the study area: (**a**) excavation-induced landslides with multiple scarps, (**b**–**d**) are landslides that are converted into debris flows; (**e**,**f**) are Google Earth images of the Bhoor Landslide and Kaptola landslide, which are deep-seated complex paleo-landslides.

A total of 789 landslides, rock falls, and debris flows were observed and recorded; the largest landslides reach about 300 m in length, 100 m in height, and an average of 15 m in depth. The smallest ones are a few meters in length, width, and depth. Out of the total area of 189.697 km^2, landslides cover a total area of 1.1369 km^2 i.e., 0.599% of the total area. The landslide inventory map is shown in Figure 5.

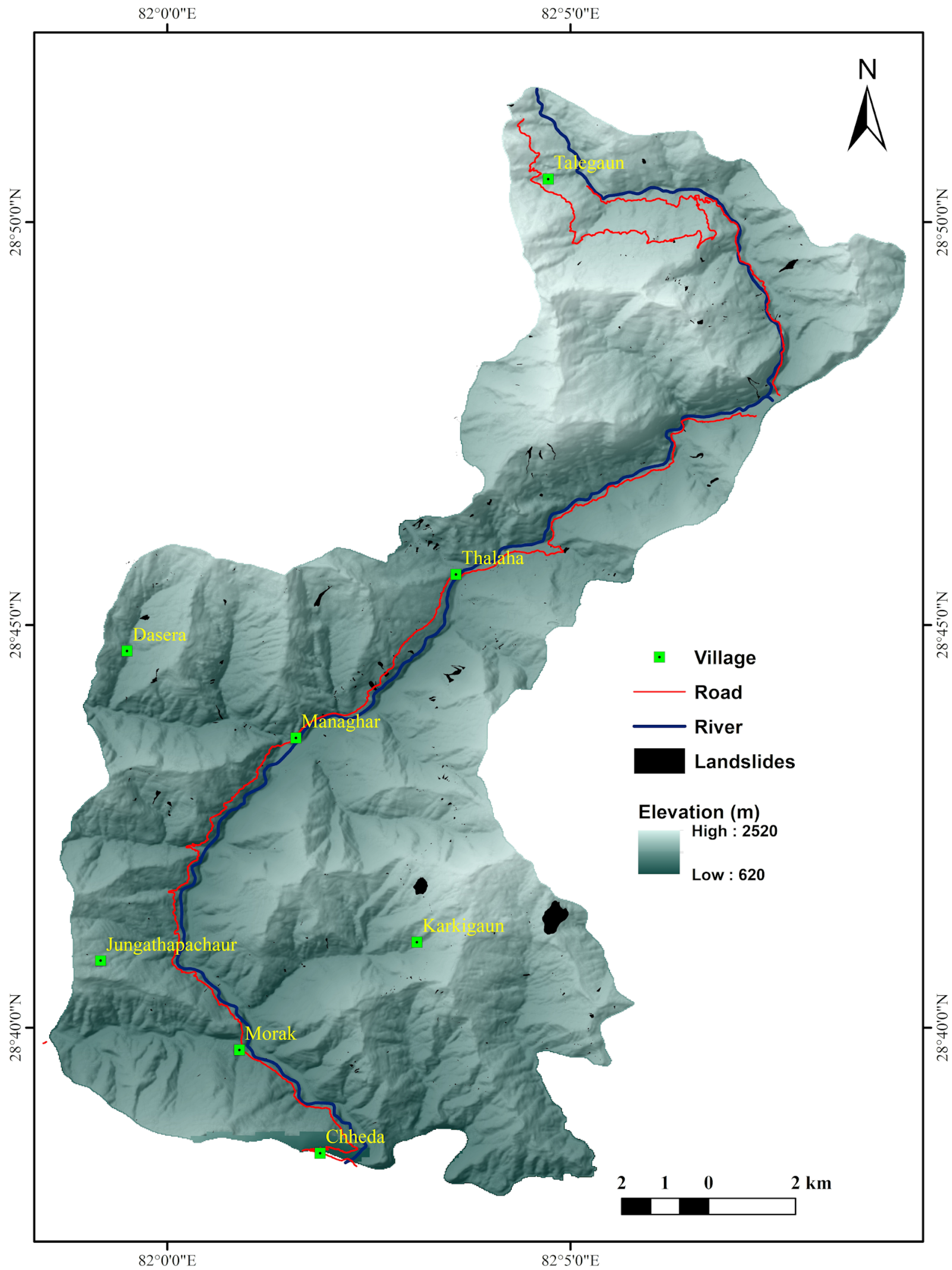

Figure 5. Landslide inventory map of the study area showing elevation ranges.

4.3. Landslide Conditioning Factors

Understanding the relationship between previous landslides and landslide contributing factors is essential for landslide susceptibility mapping. A spatial database of 13 landslide-related factors was created (Table 1, Figure 6. Later, all of the landslide conditioning factors were classified into various categories.

Table 1. The spatial relationship between each landslide-related factor and landslide locations using WOE and FR.

Factors	Weight of Evidence										Frequency Ratio			
	Total Pixel Count	Landslide Pixel Count	W^+	W^-	C	S^2 (W^+)	S^2 (W^-)	SC	C/SC	% Class Pixel	% Land-slide Pixel	FR	RF
Slope													
0–15	37,767	123	−0.608	0.039	−0.65	0.0081	0.00037	0.092	−7.00	7.96	4.35	0.55	0.09
15–25	127,475	489	−0.444	0.124	−0.57	0.0020	0.00043	0.050	−11.39	26.88	17.29	0.64	0.11
25–35	172,720	1002	−0.028	0.016	−0.04	0.0010	0.00055	0.039	−1.11	36.42	35.42	0.97	0.16
35–45	103,765	959	0.441	−0.168	0.61	0.0010	0.00053	0.040	15.28	21.88	33.90	1.55	0.26
45–55	28,795	240	0.337	−0.026	0.36	0.0042	0.00038	0.068	5.36	6.07	8.48	1.40	0.23
55–65	3589	16	−0.293	0.002	−0.29	0.0627	0.00035	0.251	−1.17	0.76	0.57	0.75	0.12
>65	130	0	-	0.000	-	-	0.00035	-	-	0.03	0.00	0.00	0.00
Aspect													
Flat	9748	29	−0.699	0.011	−0.71	0.0345	0.00035	0.187	−3.79	2.06	1.03	0.50	0.06
N	47,573	91	−1.141	0.073	−1.21	0.0110	0.00036	0.107	−11.39	10.03	3.22	0.32	0.04
NE	54,616	144	−0.820	0.0055	−0.89	0.0069	0.00037	0.086	−10.39	11.52	5.09	0.44	0.05
E	59,891	401	0.116	−0.018	0.13	0.0025	0.00041	0.054	2.48	12.63	14.17	1.12	0.13
SE	63,489	510	0.300	−0.055	0.36	0.0019	0.00043	0.049	7.23	13.39	18.03	1.35	0.16
South	62,671	549	0.387	−0.074	0.46	0.0018	0.00044	0.048	9.67	13.22	19.41	1.46	0.16
SW	66,022	579	0.388	−0.080	0.47	0.0017	0.00044	0.047	10.00	13.92	20.47	1.47	0.17
W	64,527	396	0.029	−0.005	0.033	0.0025	0.00041	0.054	0.61	13.61	14.00	1.03	0.12
NW	45,704	130	−0.744	0.055	−0.80	0.0077	0.00037	0.090	−8.88	9.64	4.60	0.48	0.06
Curvature													
<0	118,957	921	0.263	−0.106	0.37	0.0010	0.00052	0.040	9.14	25.08	32.56	1.30	0.43
0	119,461	721	0.012	−0.004	0.02	0.0014	0.00047	0.043	0.36	25.19	25.49	1.01	0.34
>0	235,823	1187	−0.171	0.145	−0.32	0.0008	0.00061	0.038	−8.25	49.73	41.96	0.84	0.28
SPI													
Low erosive	152,140	583	−0.439	−0.226	−0.21	0.0017	0.00044	0.047	−4.57	32.08	20.61	0.64	0.21
high erosive	157,321	792	−0.165	−0.324	0.16	0.0012	0.00049	0.042	3.80	33.17	28.00	0.84	0.28
very high erosive	164,780	1454	0.400	−0.719	1.12	0.0006	0.00072	0.038	29.66	34.75	51.40	1.48	0.49
TWI													
2.05–5.4	248,941	1214	0.822	−0.557	1.38	0.0008	0.00062	0.038	36.22	52.49	42.91	0.82	0.15
5.4–6.8	139,798	999	1.207	−0.432	1.64	0.0010	0.00054	0.039	41.52	29.48	35.31	1.20	0.22
6.8–8.77	55,691	456	1.384	−0.171	1.55	0.0022	0.00042	0.051	30.30	11.74	16.12	1.37	0.25
8.77–11.57	21,471	128	1.005	−0.041	1.05	0.0078	0.00037	0.091	11.53	4.53	4.52	1.00	0.18
11.57–15.59	6495	28	0.726	−0.004	0.73	0.0358	0.00035	0.190	3.83	1.37	0.99	0.72	0.13
15.59–23.51	1845	4	0.364	0.005	0.36	0.2505	0.00035	0.50	0.72	0.39	0.14	0.36	0.07
Lithology													
Badakada Formation	72,664	104	−1.427	−0.032	−1.40	0.0096	0.00037	0.100	−13.95	15.38	3.69	0.24	0.02
Baskot Marble	23,743	717	1.651	−0.289	1.94	0.0014	0.00047	0.044	44.33	5.02	25.41	5.06	0.50
Batule Formation	114,974	770	0.121	−0.314	0.44	0.0013	0.00048	0.042	10.28	24.33	27.29	1.12	0.11
Chhera Diamictite	59,485	68	−1.652	−0.019	−1.63	0.0147	0.00036	0.123	−13.30	12.59	2.41	0.19	0.02
Karkigaun Schist	19,391	260	0.822	−0.091	0.91	0.0039	0.00039	0.066	13.95	4.10	9.21	2.25	0.22
Karnali Klippe	41,794	83	−1.099	−0.024	−1.07	0.0120	0.00036	0.112	−9.64	8.84	2.94	0.33	0.03
Marka Formation	140,523	820	−0.017	−0.339	0.32	0.0012	0.00050	0.042	7.74	29.74	29.06	0.98	0.04

Table 1. *Cont.*

Factors	Weight of Evidence								Frequency Ratio			
	Total Pixel Count	**Landslide Pixel Count**	W^+	W^-	**C**	S^2 (W^+)	S^2 (W^-)	**SC**	**C/SC**	**% Class Pixel**	**% Landslide Pixel**	**FR**	**RF**
Land Use													
Barren land	5261	114	1.312	−0.024	1.34	0.0089	0.00037	0.097	13.83	1.11	1.04	0.94	0.38
Cultivation and Buildup	136,610	546	−0.396	0.132	−0.53	0.0018	0.00044	0.048	−11.07	28.81	5.01	0.17	0.07
Forest	323,200	2004	0.045	−0.083	0.13	0.0005	0.00121	0.041	3.07	68.15	18.38	0.27	0.11
Water Bodies	9159	165	1.123	−0.035	1.16	0.0061	0.00037	0.081	14.31	1.93	1.51	0.78	0.32
Thrust (m)													
0–500	26,231	245	0.456	−0.034	0.49	0.0041	0.00038	0.067	7.29	5.51	8.86	1.57	0.52
500–1000	26,825	149	−0.072	0.004	−0.08	0.0067	0.00037	0.084	−0.90	5.66	5.27	0.93	0.31
>1000	421,285	2435	−0.032	0.222	−0.25	0.0004	0.00255	0.054	−4.66	88.83	86.07	0.97	0.32
Syncline													
Close	28,999	57	−1.106	−1.014	−1.09	0.0175	0.00036	0.134	8.15	6.10	2.01	0.33	0.07
Nearby	28,009	489	1.091	−0.185	1.28	0.0020	0.00042	0.050	−25.47	5.91	17.29	2.93	0.64
Distant	417,293	2283	−0.081	−1.644	1.56	0.0004	0.00183	0.048	−32.77	87.99	80.70	0.92	0.20
Anticline													
Close	9781	137	0.868	−0.044	0.91	0.0074	0.00037	0.088	−10.36	2.06	4.84	2.35	0.54
Nearby	9729	96	0.513	−0.029	0.54	0.0105	0.00036	0.104	−5.19	2.05	3.39	1.65	0.38
Distant	454,731	2596	−0.038	−2.496	2.46	0.0003	0.00429	0.068	−35.92	95.89	91.76	0.96	0.22
Road (m)													
0–100	122,891	1364	0.626	−0.360	0.99	0.0007	0.00068	0.038	26.10	26.91	48.21	1.86	0.47
100–300	132,958	721	−0.096	0.035	−0.13	0.0013	0.00047	0.043	−3.303	28.04	25.49	0.91	0.23
300–500	86,129	407	−0.234	0.045	−0.28	0.0024	0.00041	0.054	−5.21	18.16	14.39	0.79	0.20
>500	132,263	337	−0.854	0.201	−1.06	0.0029	0.00040	0.058	−18.16	27.89	11.91	0.43	0.11
Stream (m)													
0–25	78,240	613	0.280	−0.240	0.52	0.0016	0.00045	0.046	11.35	16.50	21.67	1.31	0.32
25–50	62,086	374	0.016	−0.137	0.15	0.0026	0.00040	0.056	2.74	13.09	13.22	1.01	0.24
50–100	109,003	586	−0.099	−0.227	0.13	0.0017	0.00044	0.047	2.77	22.98	20.71	0.90	0.22
>100	224,912	1256	−0.060	−0.584	0.52	0.0008	0.00063	0.038	13.80	47.43	44.40	0.94	0.23
Precipitation (mm/yr)													
1600	52,340	94	−1.199	−0.028	−1.17	0.0106	0.00036	0.105	−11.15	11.03	3.32	0.30	0.13
1800	328,437	2259	0.149	−1.601	1.75	0.0004	0.00175	0.407	37.29	69.26	79.85	1.15	0.50
2000	93,464	476	−1.153	−1.079	0.03	0.0021	0.00042	0.050	0.52	19.70	16.83	0.85	0.37

Slope gradient is one of the principal factors affecting landslide occurrence. The slope angle distribution of the topography in the study area ranges from 0 to 69.71°, which was categorized into seven different classes: 0–15°, 15°–25°, 25°–35°, 35°–45°, 45°–55°, 55°–65°, and >65° (Figure 6a). The study revealed that the landslides are most prone to topography with the slope angles ranging from 35° to 45° having a frequency ratio of 1.55 and weightage of 0.61.

The slope aspect controls moisture retention and it is also related to the attitude of bedding of the rock formation, which in turn affects the physical properties of slope material and its susceptibility to failure [45,46]. In the present study, the slope aspect has been classified into nine different classes (Figure 6b), as flat (0), northeast (22.5°–67.5°); east (67.5°–112.5°); southeast (112.5°–157.5°); south (157.5°–202.5°); southwest (202.5°–247.5°); west (247.5°–292.5°); northwest (292.5°–337.5°); and north (337.5°–22.5°) (Figure 7b). The study revealed that the south and southwest facing slopes are more prone to landslide susceptibility (Table 1). Such slopes of the basins are typically anti-dipping slopes, where rainfall and the continuous fall of weathered debris are typical, and the south-facing landscape is typically on the windward side of the monsoon rain.

Slope erosion processes can affect slope stability, mostly in steep terrain. This process concentrates or disperses surface and subsurface water in the landscape due to slope shape, which makes slope shape a landslide causative factor [47]. The spatial distribution of slope curvature has been classified into three types: linear (−0.001–0.001), concave (−0.001), and convex (>0.001) (Figure 6c). The slope with a concave shape, also known as a convergent landform, is usually the least stable because it develops relatively high pore-water pressure, increasing the driving force due to the concentration of water in a certain area, which eventually initiates a slope failure. The study revealed that the concave shape of the slope is most susceptible to landslides. It has a weightage value of 0.36 and a frequency ratio of 1.29.

The Topographic Wetness Index (*TWI*) is an index value that reflects the tendency of water to accumulate at any point within the catchment and the tendency of gravitational forces to move that water down the slope [48]. The *TWI* is commonly used to quantify topographic control on hydrological processes [49] and can be calculated as per the equation used by Youssef et al. [50] given in Equation (6):

$$TWI = \ln\left(\frac{A}{tan\beta}\right) \tag{6}$$

where A = specific catchment area and β = slope gradient.

TWI of the topography is classified into six classes: 2.05–5.4, 5.4–6.8, 6.8–8.77, 11.57–15.59, and 15.59–23.51 (Figure 6d, Table 1). Landslides are more likely to occur in topographic features with lower *TWI* values that favor the accumulation of water (Table 1).

The stream power index (SPI) describes the erosive strength of the stream on the slope. It is a measurement of the erosive power of flowing water based on the assumption that discharge is proportional to specific catchment area [50]. It can be calculated as:

$$\mathrm{SPI} = (\tan \beta \times \mathrm{A_s})$$

where β = slope angle in degree.

$\mathrm{A_s}$ can be estimated by using the approach introduced by Hengl et al. [51] as:

$$\mathrm{A_s} = (\mathrm{A_m} \times \mathrm{P}^2/\Sigma_{\mathrm{Li}})$$

where P = pixel size, $\mathrm{A_m}$ = sum of drainage fraction from surrounding, $\sum_{\mathrm{Li}}$ = total length of drainage pixels.

In the present study, three classes are considered: (1) low erosive; (2) high erosive; and (3) very high erosive (Figure 6e). The study showed that, as per the calculated weights, the very high erosive class comparatively contributes the most to landslides.

Stream proximity is the distance from the location of interest to the nearest stream. The closeness of stream or natural drainage has an important effect on slope stability [52]. For the present study, stream proximity is categorized into four classes: (1) 0–25 m; (2) 25–50 m; (3) 50–100 m; and (4) >100 m (Figure 7f). The landforms close to the stream i.e., within the proximity of 25 m are most susceptible to the events of mass movement (Table 1). Stream proximity appeared to be a major landslide contributing factor with significant weightage. Similarly, the distance from road alignments also appeared to be one of the contributing factors for the landslide occurrences.

The properties of the rock units and geological structure within the study area are important factors in landslide occurrence [52,53]. Depending on the characteristics and types, different rock units have varying attitudes toward landslides. The major rock types in the study area are schist, diamictite-schist, phyllite, and quartzite, with frequent basic intrusions (Figure 7). All the rock types in the study area are highly deformed, fractured, and weathered due to the presence of weathering-sensitive minerals such as micas and feldspar (Figure 7).

The majority of the area is covered by ductile incompetent rocks such as schist, meta-diamictite, and phyllites. They have undergone folding during various stages of Himalayan deformation. Furthermore, even competent rocks, such as quartzite and marble, are highly fractured and brecciated. Quartzite and marble are intercalated with incompetent rocks, such as phyllite and schists. This stratigraphic arrangement is prone to differential weathering. The Thabang Formation, which has interbedded marble and schist, and the Chaurjhari Formation, which has incompetent lithology, are the most prone to landslides (Figure 6g, Table 1).

Furthermore, the presence of a fault decreases the rockmass strength, thereby increasing the landslide susceptibility; faults also play an important role in abnormal groundwater conditions as there is high water seepage through the fault or even significant water flow can occur along fault line which can saturate the slopes and eventually trigger landslides [37,54,55]. Therefore, faults are one of the major landslides contributing factors. A digital thematic distance from faults map was prepared and classified into three classes: (1) 0–500 m; (2) 500–1000 m; and (3) >1000 m (Figure 6h). Table 1 shows that the areas closer to the faults are more susceptible to landslide occurrences.

Geological structures formed by both brittle and ductile deformation break the homogeneity of rock mass and reduce the shear strength. Likewise, the area closer to the fold's axis is weaker and is also susceptible to landslides. The study area has one large-scale/regional syncline fold axis and one anticline fold axis. Furthermore, many small-scale anticline and syncline folds contribute to the instabilities. A digital thematic distance from syncline and anticline map was created and classified into three categories: close (0–100 m); nearby (100–500 m); and distant (>500 m) (Figure 6i,j).

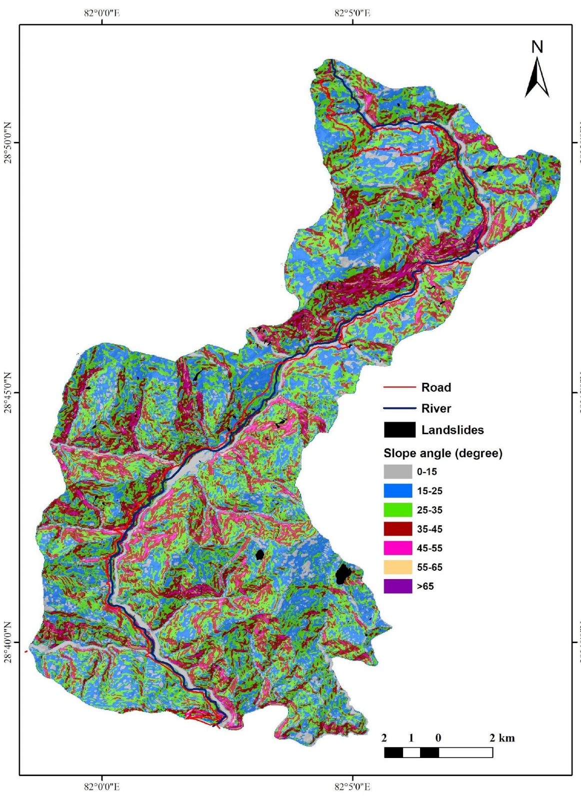

(**a**)

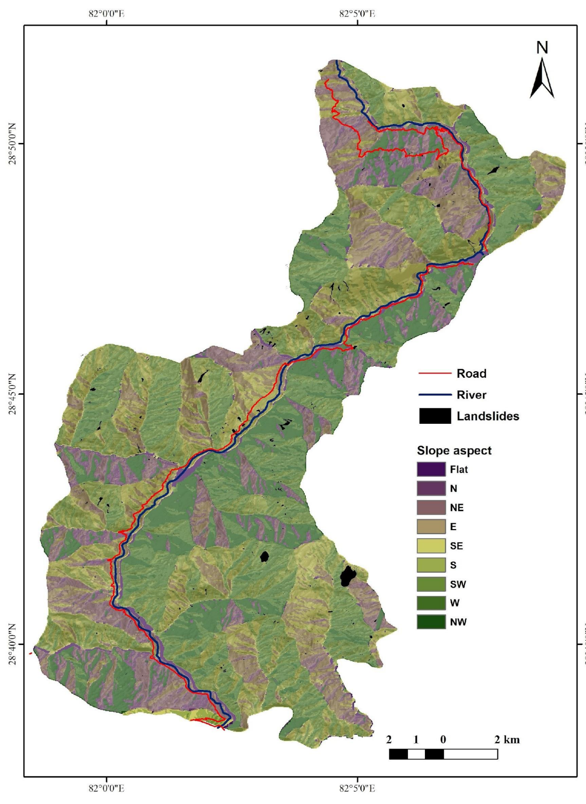

(**b**)

Figure 6. *Cont.*

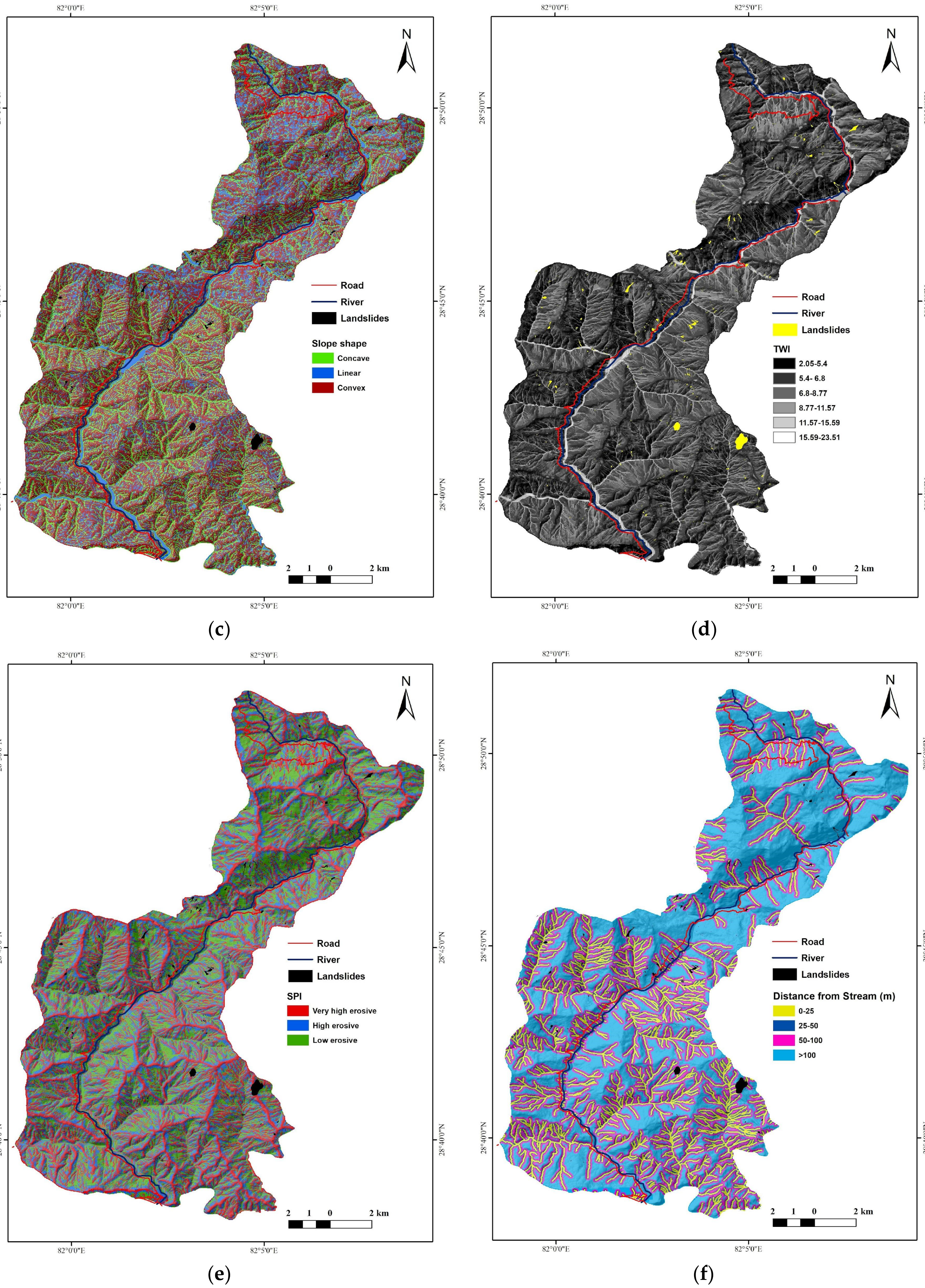

Figure 6. *Cont.*

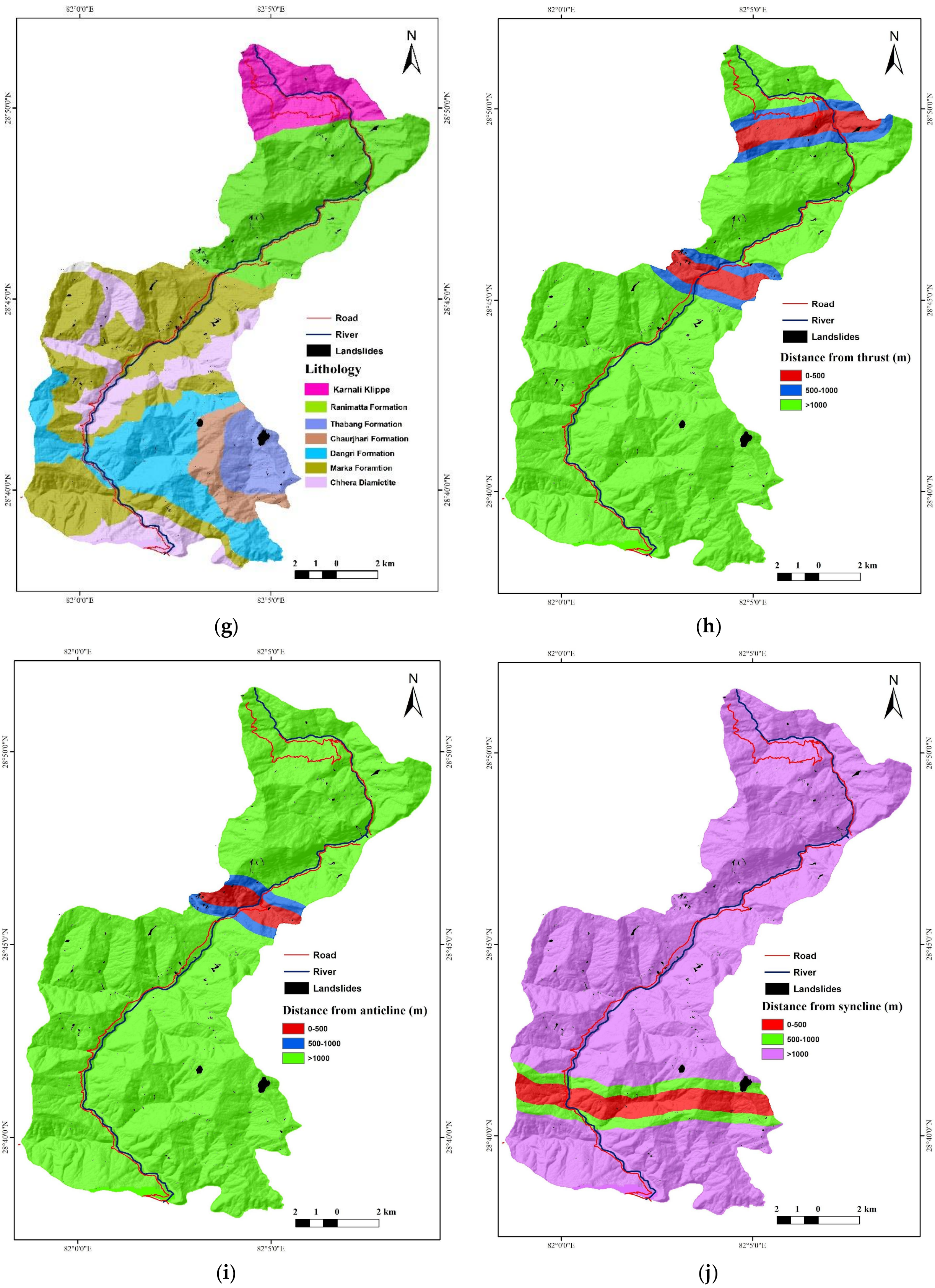

Figure 6. *Cont.*

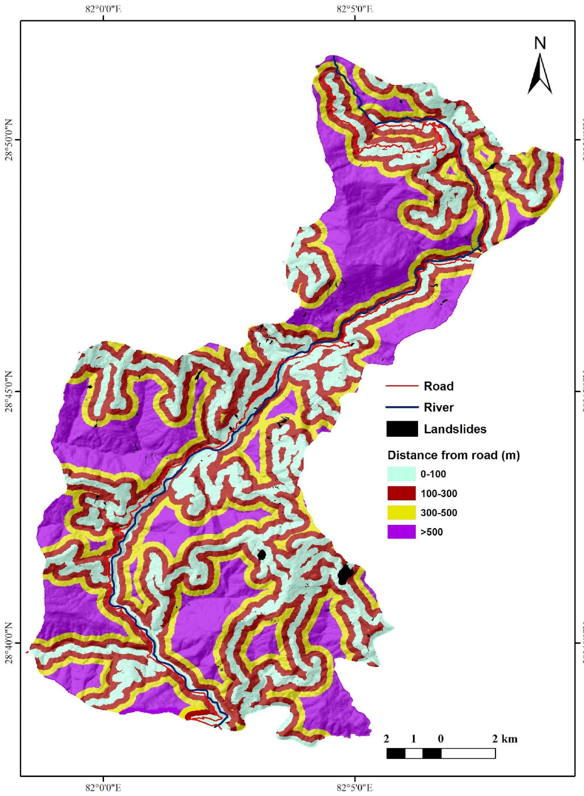

(**k**)

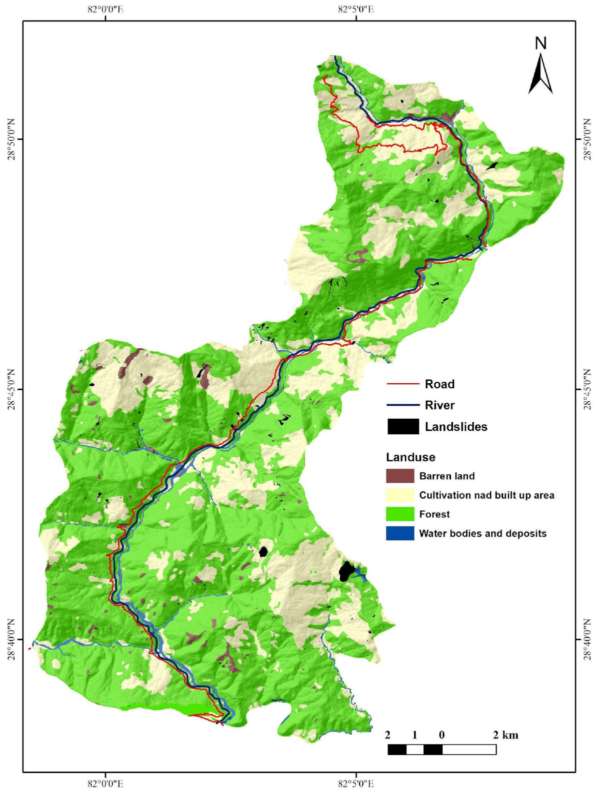

(**l**)

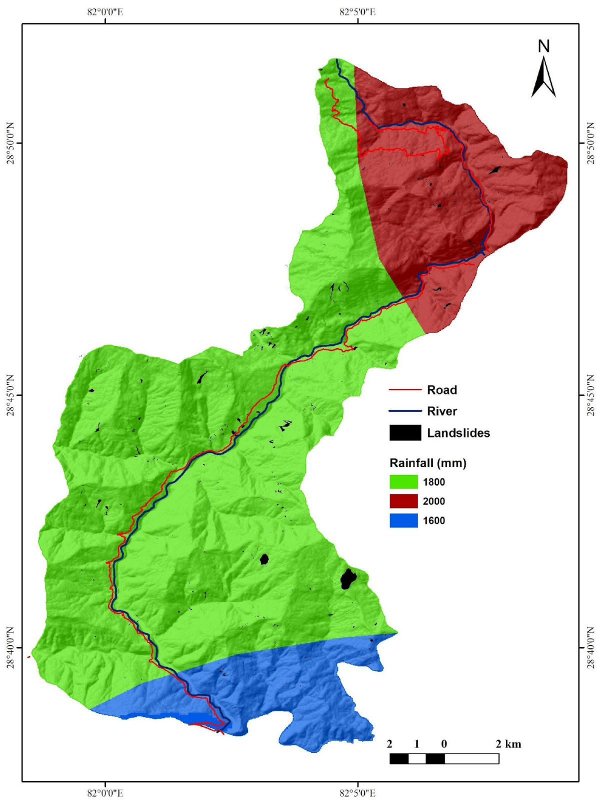

(**m**)

Figure 6. Landslide conditioning factor maps of the study area: (**a**) slope angle; (**b**) slope aspect; (**c**) slope shape, (**d**) TWI; (**e**) SPI; (**f**) stream proximity; (**g**) lithology (**h**) distance from thrust; (**i**) distance from major anticline; (**j**) distance from major syncline; (**k**) distance from the road; (**l**) land use; and (**m**) precipitation.

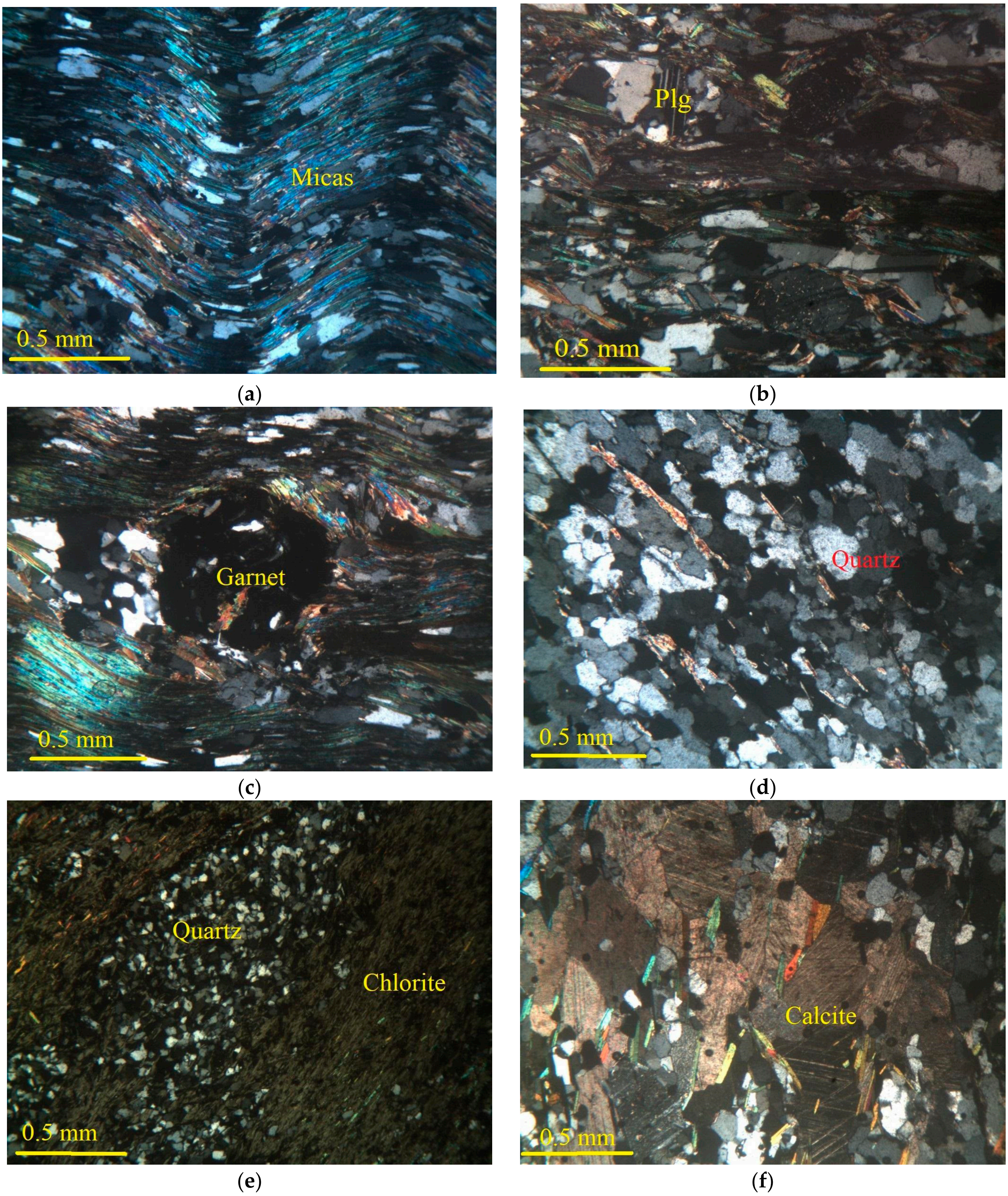

Figure 7. Photomicrographic reference of representative rock samples from the study area: (**a**) schist; (**b**) meta-diamictite; (**c**) garnetiferous schist; (**d**) micaceous quartzite; (**e**) amphibolite (meta-basic rocks); and (**f**) siliceous marble. plg = plagioclase feldspar.

Furthermore, land use can alter soil microbiological processes and have an impact on slope stability. It is classified into four categories in the current study based on data provided by Nepal's Department of Survey (DOS): (1) barren lands; (2) cultivation and built-up area; (3) forest; and (4) water bodies and deposits. Figure 6l and Table 1 show that barren lands are most susceptible to landslides.

Lastly, rainfall is a major triggering agent of landslides in mountainous terrain [6,12]. When daily precipitation exceeds 144 mm, the likelihood of a landslide occurring in the Himalayas increases significantly [56]. The annual precipitation in the area ranges from 1600 mm to 2000 mm [32]. This factor is classified into three classes in the current study: 600 mm, 1800 mm, and 2000 mm (Figure 6m). According to the results of the in situ permeability tests, the coefficients of permeability (K), transmissivity (T), and storativity (S) for old colluvium materials are 1.88×10^{-2} m/s, 6.2×10^{-2} m^2/sec, and 0.588, respectively. Likewise, the values of K, T, and S for residual soils are 2.73×10^{-4} m/s, 0.091 m^2/sec, and 0.3841, respectively, and that for weathered bedrock are 5.62×10^{-5} m/s, 1.68×10^{-3} m^2/sec, and 0.7248, respectively. With a significant amount of rainfall, the coefficients of permeability, storativity, and transmissivity of all these material categories are quite significant, and enough water could infiltrate to downslope which has incompetent rocks like schists and intercalation of incompetent and competent rocks like quartzite and schists. This process can lead to differential weathering in rocks and an increment in pore water pressure below the surface, which contributes to landslides.

Road construction can disturb the slopes, increasing the possibility of a landslide [57]. During the field survey, several landslides were observed along the roadside. A digital thematic distance from a road map was prepared for the present study and classified into four classes: (1) 0–100 m; (2) 100–300 m; (3) 300–500 m; and (4) greater than 500 m (Figure 6k). Calculation during landslide susceptibility modeling revealed that the area nearer to the road is more susceptible to landslides.

4.4. Landslide Susceptibility Modeling

The process of statistical approach combined with geo-mechanical understanding can be a powerful tool for landslide susceptibility modeling. The prior probability and the posterior probability are the major principles of the WOE [58]. Calculation of the ratio of the probability of occurrence to non-occurrence of landslides for a given set of an attribute is the major working principle for the FR. In the present research, the FR and WOE methods were used to determine the level of correlation between the location of landslides and landslide-conditioning factors. Prior probability was calculated first by the probability of an event of the same type occurring in the previous period, and then the same probability was used for an event's future probability. The detailed results of the susceptibility assessment are shown in Table 1, including the spatial relationship between landslide and landslide contributing factor classes for both the FR and the WOE models.

The landslide susceptibility index (LSI) values for the WOE method varies from -1.45 to 13.22 and that for the FR ranges from 201 to 456. There is no general rule for susceptibility zone division. In the present study, the LSI index map from both approaches is categorized into very low, low, moderate, high, and very high susceptibility classes in such a way that each class has nearly equal area distribution (around 20%) based on LSI values. Table 2 shows the percentage distribution of overall area coverage by very low, low, medium, high, and very high susceptibility class and landslide distribution within each class. Figure 8 shows the landslide susceptibility models developed using the FR and the WOE methods.

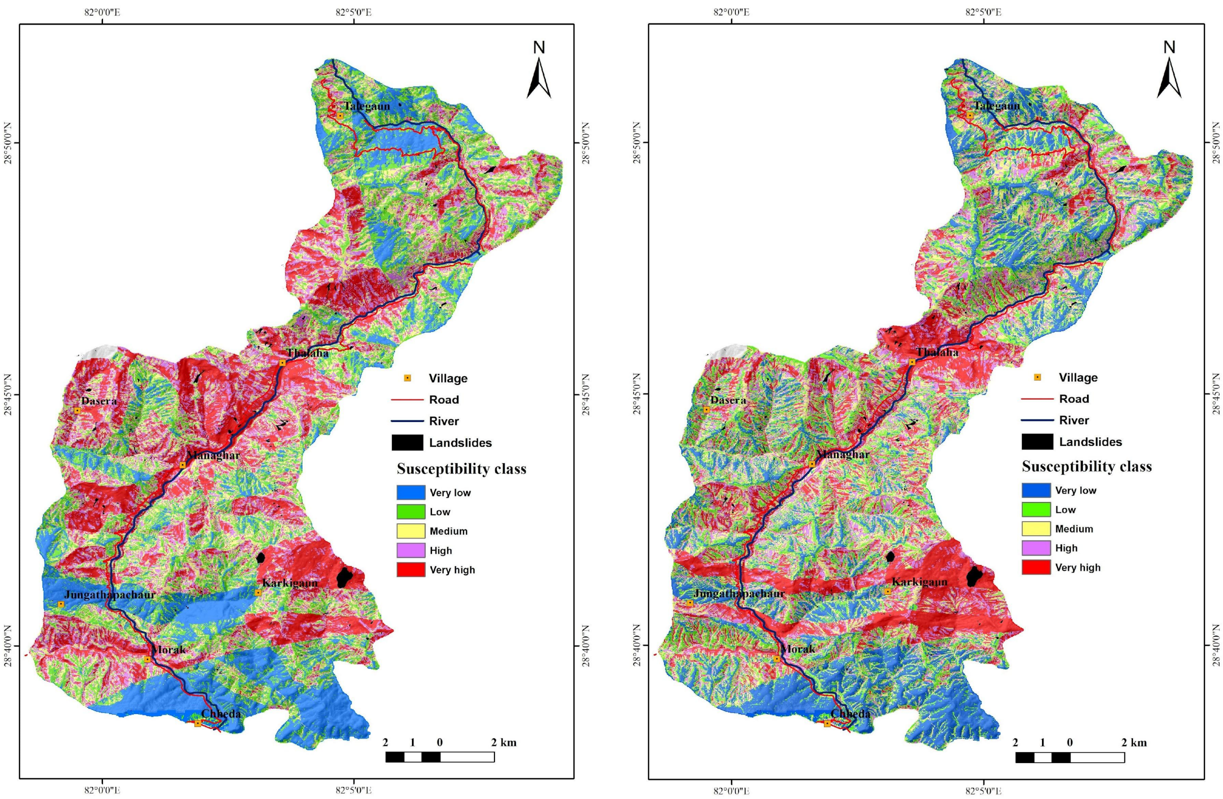

(**a**) (**b**)

Figure 8. Landslide susceptibility models prepared using: (**a**) WOE method, (**b**) FR method.

Table 2. Observed landslide density in the different susceptibility zones of the landslide susceptibility zonation map.

Method	Susceptibility Zones	Total Area (sq. km)	Total Area%	Landslide Area in Zones (sq. km)	Landslide Area%	Landslide Density	Degree of Fit (%)
FR	Very low	38.51	20.37	0.03	2.80	0.14	2.70
	Low	39.03	20.65	0.08	7.51	0.36	7.14
	Medium	37.30	19.73	0.11	10.10	0.51	10.05
	High	37.50	19.84	0.22	19.17	0.97	18.98
	Very High	36.68	19.41	0.68	60.42	3.11	61.13
WOE	Very low	36.11	19.11	0.04	3.12	0.16	3.36
	Low	38.32	20.28	0.06	5.07	0.25	5.14
	Medium	36.60	19.37	0.11	9.39	0.48	9.97
	High	38.48	20.36	0.18	15.80	0.78	15.96
	Very High	39.47	20.89	0.75	66.62	3.19	65.58

4.5. Validation

Two basic assumptions are needed for the validation of landslide susceptibility maps: landslides are related to spatial information such as topography and geology, and future landslides will occur by a specific trigger, such as rainfall or an earthquake [59,60]. In the present study, these two necessary conditions are fulfilled as landslides are related to all the spatial information and they are also triggered by rainfall.

In the present case, approximately 80% of the recorded landslides are within high and very high susceptibility zones for both FR and WOE models. To evaluate the overall quality of the landslide susceptibility map, it is also necessary to compute the landslide density of each class [61]. The landslide density for the very high susceptible zone is 3.11 for the FR and 3.18 for the WOE, which is significantly higher than the landslide density for the other susceptible zones. There is a gradual decrease in landslide density from the very high to lower landslide susceptible zones, with significant differences in the values between the different susceptible zones (Table 2). These results are consistent with the field observations.

The validity of the landslide susceptibility map can also be estimated graphically and quantitatively using the success rate curve [59,62]. For the success rate curve, the cumulative percentage of observed landslide occurrence is plotted against the areal cumulative percentage in decreasing LSI values (Figure 9). The area under a curve for the WOE method is 0.7942, while that for the FR method is 0.7762, resulting in an overall success rate of 79.42% and 77.62%, respectively. This result also validates the landslide susceptibility map with the pre-existing slope instability conditions.

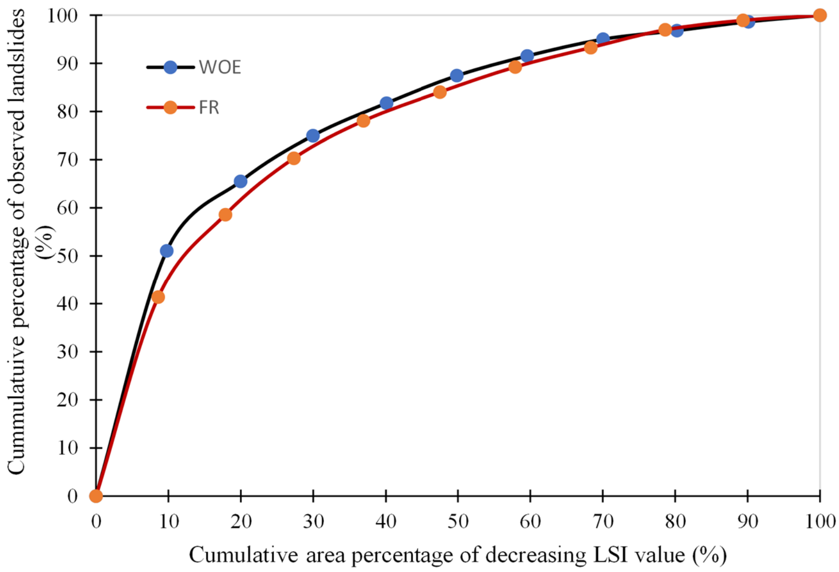

Figure 9. Success rate curve showing cumulative percentage of observed landslide occurrences versus cumulative percentage of decreasing landslide susceptibility index value.

5. Discussion

For the present research, we considered the region between Chhedachaur to Saureni, the Southern part of Jajarkot district, Nepal. Despite an exploration of the area by many researchers, uniformity in the geological map of the area was lacking, due to which a detailed geological investigation was conducted as the first step. Moreover, there is still some confusion about the boundary of these two crystalline bodies. As we did not find any traces of the root zone within the study area, we support the concept of Klippe following the work of Dhital [35]. The detailed geodynamic studies give information on the placement of crystalline bodies [63–66], however there are no studies carried out related to geodynamics and research that incorporate geodetic data with crustal deformation in the study area.

The geological investigation included a detailed field survey, both along and across strike through many routes to delineate the lithological and tectonic boundary, which is later verified by petrographic analysis. The area revealed three tectonostratigraphic successions: the Karnali Klippe, the Lesser Himalaya, and the Jajarkot Klippe, most of which have their own well-defined litho-stratigraphic successions. The litho-stratigraphic subdivision of the rock sequences of the present work can be correlated with the work of Fuchs [67], Sharma et al. [68], and Stocklin [69], who have worked within, nearby, or in similar tectonic settings (Table 3). The outcome of this research is not in agreement with the recently published map of the Department of Mines and Geology, Nepal [70], in terms of structural boundaries and litho-stratigraphy.

Table 3. Litho-stratigraphic correlation of rock succession of the present study area with other existing literature.

Present Observation		**Hagen (1969) [39]**	**Fuchs (1974) [67]**	**Sharma et al. (1984) [68]**		**Stocklin (1980) [69]**		**Dhital (2015) [40]**	
Karnali Klippe	Higher Himalayan Rocks	Kathmandu Nappe	Upper Crystalline Nappe						
MCT		—							
Lesser Himalaya	Ranimatta Formation	Hiunchuli Zone	Chail Nappe					Ranimatta Formation	
–Thalaha Thrust (TT)–		—-							
Jajarkot Klippe	Thabang Formation	Jajarkot Nappe 1	Lower Crystalline Nappe	Chaurjhari Group	Thabang Formation	Bhimphedi Group	Bhainseddoban Marble	Higher Himalayan Crystallines	
	Chaurjhari Formation				Chaurjhari Formation		Raduwa Formation		
								—-MCT—	
	Dangri Formation	Hiunchuli Zone and Piuthan Zone (?)	Chail Nappe	-Marma Khola Thrust- Kuncha Group		—Mahabharat Thrust—		Sharda Group	Dangri Formation
								—-Kapurkot Thrust—-	
	Marka Formation with Chhera Diamictite member							Dailekh Group	Marka Formation
									Chhera Diamictite
									Ranimatta Formation

In the second step, the spatial distribution pattern of the landslides was carried out. Most of the landslides were observed near the thrust and fold axis, close to roads and stream, within the formation comprising of inter-bedding of competent and incompetent lithology, and within the south and south-west dipping slopes having slope angles of 35°–45°. The most important observation was that fresh shallow landslides were observed along the road alignment, which is most probably due to the haphazard excavation of the road without geological and geotechnical consideration. In addition, the reduction of the shear strength by the development and/or propagation of the geological structures, and the differential weathering of the rock mass, contributed the most to the occurrence of landslides.

An important step to assess the landslide susceptibility is the selection of the predisposing factors, the understanding of their combined effects, and the relative importance of the selected factors on landslide distribution [71]. So, in the third step, landslide susceptibility modeling was carried out employing two different methods i.e., the WOE and the FR, by considering the 13 causative factors of slope angle, slope aspect, slope shape, SPI, TWI, lithology, distance from thrust, distance major syncline, distance from major anticline, stream proximity, distance from the road, land use, and mean annual precipitation. The statistical analysis results showed that the models performed well, as evidenced by the degree of fit and the percentage of occurrences of landslides in each susceptibility class. The high and very high susceptibility classes have a higher degree of fit, which decreases significantly towards the lower susceptibility class. Furthermore, the success rate obtained is good (79.42% for the WOE approach and 77.62% for the FR approach). Other studies also reported the success rate within this proximity, for example Dahal et al. [72] reported a success rating of 77.6% to 80.66% from the WOE method. Kayastha et al. [31] reported a success rate of 79% from the WOE method. KC et al. [37] found 75% and 71% success rates for the WOE and FR methods, respectively, from the research in Arun Tectonic Window, Nepal. Bijukchhen et al. [73] have reported a success rate of around 80% from the heuristic and bivariate statistical methods. Akgun [74] reported the success rate of logistic regression, frequency ratio, and analytical hierarchy process (AHP) methods at 81%, 76%, and 71%, respectively.

Some of the previous studies have concluded that the WOE method produced better results than the FR method [37,75], and the same is true for the current study area. The results show that the FR and WOE models are suitable for this study and can be successfully applied to landslide susceptibility zonation mapping in other mountainous areas with similar topographical and physical features.

6. Conclusions

In this study, detailed geologial investigation is carried out to develop the precise geological map of the southen part of Jajarkot district in between the two crystalline zones i.e., Karnali Crystalline Zone and Jajarkot Crystalline Zone, Nepal. Investigation on whether these crystalline bodies are klippen or nappes is performed. Furthermore, extensive survey on landslide distribution pattern in the area is conducted along with the landslide susceptibility mapping using two bivarate models i.e., Frequency Ratio (FR) and Weight of Evidence (WOE), considering 13 causative factors. The major findings of this study are listed below:

- From detailed geological exploration, a new geological map of the study area is developed, which can be the reference for further research in this area. This map can be crucial for the planning of infrastructure development.
- This study supports the concept that the crystalline bodies i.e., Karnali Crystalline Zone and Jajarkot Crystalline Zone, located around the study area are klippen.
- The field survey shows that the haphazard road excavation without the consideration of geological and geotechnical features of the site has caused rampant shallow landslides.
- Susceptibility modeling using both the FR and the WOE methods shows that the lithology is the most important conditioning factor for landslide occurrence, while, land use, distance from geological structures, road, SPI, slope, aspect and TWI, have played a moderate role.
- The overall success rating of the FR and WOE method in the study area are 77.62% and 79.42%, respectively, with the 13 causative factors considered. The development of such susceptibility maps under similar geoenvironmental and topographical features, as in this study, and considering similar causative factors, can be useful for the mitigation of landslide hazards in other places of the world.

Author Contributions: Conceptualization, Y.B.S. and S.K.; methodology, D.K., H.D., Y.B.S., S.K. and G.A.; software, S.K., D.K. and H.D.; formal analysis, Y.B.S., S.K., D.K., H.D. and K.R.P.; investigation, Y.B.S., S.K. and G.A.; resources, K.R.P.; data curation, Y.B.S., S.K., G.A., D.K. and H.D.; writing—original draft preparation, Y.B.S., S.K., G.A., D.K. and H.D. writing—review and editing, D.K., S.K. and H.D.; visualization, Y.B.S., S.K., G.A. and H.D.; supervision, D.K. and K.R.P.; project administration, K.R.P. All authors have read and agreed to the published version of the manuscript.

Funding: This research received no external funding.

Data Availability Statement: Data used in the present study is contained within the article.

Acknowledgments: The authors would like to thank Pawan Kumar Acharya and Aneeta Thapa for their cooperation and support during the field study.

Conflicts of Interest: The authors declare no conflict of interest.

References

1. Jaeger, J.; Courtillot, V.; Tapponnier, P. Paleontological view of the ages of the Deccan Traps, the Cretaceous/Tertiary boundary, and the India-Asia collision. *Geology* **1989**, *17*, 316–319. [CrossRef]
2. Besse, J.; Courtillot, V.; Pozzi, J.P.; Westphal, M.; Zhou, Y.X. Palaeomagnetic estimates of crustal shortening in the Himalayan thrusts and Zangbo suture. *Nature* **1984**, *311*, 621–626. [CrossRef]
3. Copley, A.; Avouac, J.-P.; Royer, J.-Y. India–Asia collision and the Cenozoic slowdown of the Indian plate: Implications for the forces driving plate motions. *J. Geophys. Res.* **2010**, *115*, 1–14. [CrossRef]
4. Avouac, J.-P. Mountain building, erosion and the seismic cycle in the Nepal Himalaya. *Adv. Geophys.* **2003**, *46*, 1–80.

5. Searle, M.P. Structural evolution and sequence of thrusting in the High Himalayan, Tibetan-Tethys and Indus suture zones of Zanskar and Ladakh, Western Himalaya. *J. Struct. Geol.* **1986**, *8*, 923–936. [CrossRef]
6. Pratt-Sitaula, B.; Burbank, D.W.; Heimsath, A.; Ojha, T. Landscape disequilibrium on 1000–10,000 year scales Marsyandi River, Nepal, central Himalaya. *Geomorphology* **2004**, *58*, 223–241. [CrossRef]
7. Guzzetti, F. Landslide Hazard and Risk Assessment. Ph.D. Thesis, Rheinischen Friedrich Wilhelms-University Bonn, Bonn, Germany, 2005.
8. CRED. *The Human Cost of Natural Disasters 2015—A Global Perspective*; CRED; UNISDR: Brussels, Belgium, 2015; p. 55.
9. Herath, S.; Wang, Y. Case studies and national experiences. In *Landslides–Disaster Risk Reduction*; Springer: Berlin/Heidelberg, Germany, 2009; pp. 475–497.
10. Cruden, D.M. A simple definition of a landslide. *Bull. Int. Assoc. Eng. Geol.* **1991**, *41*, 27–29. [CrossRef]
11. Crosta, G.B.; Frattini, P. Rainfall-induced landslides and debris flows. *Hydrol. Process.* **2008**, *22*, 473–477. [CrossRef]
12. Cannon, S.H.; Bigio, E.R.; Mine, E. A process for fire-related debris flow initiation, Cerro Grande fire, New Mexico. *Hydrol. Process.* **2001**, *15*, 3011–3023. [CrossRef]
13. Fannin, R.J.; Rollerson, T.P. Debris flows: Some physical characteristics and behaviour. *Can. Geotech. J.* **1993**, *30*, 71–81. [CrossRef]
14. Iverson, R.M.; Reid, M.E.; LaHusen, R.G. Debris flow mobilization from landslides. *Annu. Rev. Earth Planet Sci.* **1997**, *25*, 85–138. [CrossRef]
15. Dangi, H.; Bhattarai, T.N.; Thapa, P.B. An approach of preparing earthquake induced landslide hazard map: A case study of Nuwakot District, central Nepal. *J. Nepal Geol. Soc.* **2019**, *58*, 153–162. [CrossRef]
16. Dahal, B.K.; Dahal, R.K. Landslide hazard map: Tool for optimization of low-cost mitigation. *Geoenviron. Disasters* **2017**, *4*, 8. [CrossRef]
17. KC, D.; Dangi, H.; Naqvi, M.W.; Hu, L. Landslide Mobilized Debris Flow at Kalli Village in Achham, Nepal: A Case Study. In Proceedings of the 2021 ASEE North Central Section Conference, Toledo, OH, USA, 19 March 2021.
18. Joshi, I.; Chaudhary, R.K.; Diwakar, K.C. Engineering Perspective of Melamchi Disaster and Mitigation Methods. *Zenodo* **2021**, 1–4. [CrossRef]
19. KC, D.; Gautam, K.; Dangi, H.; Kadel, S.; Hu, L. Challenges in Tunneling in the Himalayas: A Survey of Several Prominent Excavation Projects in the Himalayan Mountain Range of South Asia. *Geotechnics* **2022**, *2*, 802–824. [CrossRef]
20. Devkota, K.C.; Regmi, A.D.; Pourghasemi, H.R.; Yoshida, K.; Pradhan, B.; Ryu, I.C.; Althuwaynee, O.F. Landslide susceptibility mapping using certainty factor, index of entropy and logistic regression models in GIS and their comparison at Mugling–Narayanghat road section in Nepal Himalaya. *Nat. Hazards* **2013**, *65*, 135–165. [CrossRef]
21. Van Westen, C.J.; Van Asch, T.W.; Soeters, R. Landslide hazard and risk zonation—Why is it still so difficult? *Bull. Eng. Geol. Environ.* **2006**, *65*, 167–184. [CrossRef]
22. Kayastha, P.; Dhital, M.R.; De Smedt, F. Landslide susceptibility mapping using the weight of evidence method in the Tinau watershed, Nepal. *Nat. Hazards* **2012**, *63*, 479–498. [CrossRef]
23. Anbalagan, R. Landslide hazard evaluation and zonation mapping in mountainous terrain. *Eng. Geol.* **1992**, *32*, 269–277. [CrossRef]
24. Fuchs, G.; Frank, W. The geology of west Nepal between the rivers Kali Gandakiand Thulo Bheri. *Geol. Bundesanst.* **1970**, *18*, 1–103.
25. Arita, K.; Shiraishi, K.; Hayashi, D. Geology of western Nepal and a comparison with Kumaun, India. *Bull. Fac. Sci. Hokkaido Univ.* **1984**, *21*, 1–20.
26. Dhital, M.R. Juxtaposition of Greater and Lesser Himalayan nappes in west Nepal: Implications for delineating Main Central Thrust. *Himal. Geol.* **2022**, *43*, 231–240.
27. La Roche, R.S.; Godin, L.; Crowley, J.L. Reappraisal of emplacement models for Himalayan external crystalline nappes: The Jajarkot klippe, western Nepal. *Bull. Geol. Soc. Am.* **2018**, *130*, 1041–1056. [CrossRef]
28. Yoneshiro, T.; Kizaki, K. Metamorphism and thermal structure of the Karnali Klippe, western Nepal Himalaya. *Bull. Dep. Geol.* **1996**, *5*, 1–20.
29. Hayashi, D.; Fujii, Y.; Yoneshiro, T.; Kizaki, K. Observations on the geology of the Karnali region, west Nepal. *J. Nepal Geol. Soc.* **1984**, *4*, 29–40.
30. Wang, H.B.; Sassa, K. Comparative evaluation of landslide susceptibility in Minamata area, Japan. *Environ. Geol.* **2005**, *47*, 956–966. [CrossRef]
31. DOS. *Topographic Maps of Nepal*; Department of Survey: Kathmandu, Nepal, 1996.
32. DHM. *Precipitation Map of Nepal*; Department of Hydrology and Meterology: Kathmandu, Nepal, 2021.
33. Bonham-Carter, G.F.; Agterberg, F.P.; Wright, D.F. Integration of geological datasets for gold exploration in Nova Scotia. *Photogramm. Eng. Remote Sens.* **1988**, *54*, 1585–1592.
34. Bonham-Carter, G.F. Weights of evidence modelling: A new approach to mapping mineral potential. In Statistical Applications in the Earth Sciences. *Geol. Surv. Can.* **1989**, *8–9*, 171–183.
35. Lee, S.; Ryu, J.H.; Won, J.S.; Park, H.J. Determination and application of the weights for landslide susceptibility mapping using an artificial neural network. *Eng. Geol.* **2004**, *71*, 289–302. [CrossRef]
36. Bonham-Carter, G.F. *Geographic Information Systems for Geoscientists: Modeling with GIS*; Pergamon Press: New York, NY, USA, 1994; p. 398.

37. KC, D.; Dangi, H.; Hu, L. Assessing Landslide Susceptibility in the Northern Stretch of Arun Tectonic Window, Nepal. *Civ. Eng.* **2022**, *3*, 525–540. [CrossRef]
38. Kansakar, D.R.; Chitrakar, G.R. Report on Geology of the Bheri River Section. *Dep. Mines Geol. Kathmandu* **1984**, *Unpublished*.
39. Hagen, T. Report on the Geological survey of Nepal, Vol. 1: Preliminary reconnaissance. Denkschriften der Schweizerischen Naturforschenden Gesellschaft Memoires de la Societe Helvetique des Sciences Naturelles. 1969; Volume 84, p. 185.
40. Dhital, M.R. *Geology of the Nepal Himalaya: Regional Perspective of the Classic Collidedorogen*; Springer: Berlin/Heidelberg, Germany, 2015; p. 487.
41. Dhital, M.R.; Kizaki, K. Lithology and Stratigraphy of the Northern Dang, Lesser Himalaya. *Bull. Coll. Sci. Univ. Ryukyus Okinawa* **1987**, *45*, 183–244.
42. Adhikary, T.P.; Sharma, T. Geological Report of Marma, Chaurjhari, and Jajarkot Area (Far Western Nepal). *Dep. Mines Geol. Kathmandu* **1983**, *Unpublished*.
43. Stöcklin, J.; Bhattarai, K.D. Geology of the Kathmandu Area and Central Mahabharat Range, Nepal Himalaya. *Dep. Mines Geol. UNDP* **1977**, *Unpublished*.
44. Paudyal, K.R.; Paudel, L.P. Geological study and root zone interpretation of the Kahun Klippe, Tanahun, and central Nepal. *Himal. Geol.* **2013**, *34*, 93–106.
45. Dai, F.C.; Lee, C.F.; Li, J.X.Z.W.; Xu, Z.W. Assessment of landslide susceptibility on the natural terrain of Lantau Island, Hong Kong. *Environ. Geol.* **2001**, *40*, 381–391.
46. Ghimire, M. Landslide occurrence and its relation with terrain factors in the Siwalik Hills, Nepal: Case study of susceptibility assessment in three basins. *Nat. Hazards* **2011**, *56*, 299–320. [CrossRef]
47. Nefeslioglu, H.A.; Sezer, E.B.R.U.; Gokceoglu, C.; Bozkir, A.S.; Duman, T.Y. Assessment of landslide susceptibility by decision trees in the metropolitan area of Istanbul, Turkey. *Math. Probl. Eng.* **2010**, *2010*, 901095. [CrossRef]
48. Moore, I.D.; Grayson, R.B. Terrain-based catchment partitioning and runoff prediction using vector elevation data. *Water Resour. Res.* **1991**, *27*, 1177–1191. [CrossRef]
49. Sörensen, R.; Zinko, U.; Seibert, J. On the calculation of the topographic wetness index: Evaluation of different methods based on field observations. *Hydrol. Earth Syst. Sci.* **2006**, *10*, 101–112. [CrossRef]
50. Youssef, A.M.; Pourghasemi, H.R.; El-Haddad, B.A.; Dhahry, B.K. Landslide susceptibility maps using different probabilistic and bivariate statistical models and comparison of their performance at Wadi Itwad Basin, Asir Region, Saudi Arabia. *Bull. Eng. Geol. Environ.* **2015**, *75*, 63–87. [CrossRef]
51. Hengl, T.; Gruber, S.; Shrestha, D.P. *Digital Terrain Analysis in ILWIS*; International Institute for Geo-Information Science and Earth Observation Enschede: Enschede, The Netherlands, 2003; p. 56.
52. Duman, T.Y.; Çan, T.; Emre, O.; Keçer, M.; Doğan, A.; Ateş, Ş.; Durmaz, S. Landslide inventory of northwestern Anatolia, Turkey. *Eng. Geol.* **2005**, *77*, 99–114. [CrossRef]
53. Yalcin, A. An Investigation on Ardesen (Rize) Region on the Basis of Landslide Susceptibility. Ph.D. Thesis, Karadeniz Technical University, Trabzon, Turkey, 2005.
54. Leir, M.; Michell, A.; Ramsay, S. Regional landslide hazard susceptibility mapping for pipelines in British Columbia. Geo-engineering for the society and its environment. In Proceedings of the 57th Canadian Geotechnical Conference and the 5th Joint CGS-IAH Conference, Waterloo, ON, Canada, 24–27 October 2004; pp. 1–9.
55. Chen, Y.; Yu, J.; Shahbaz, K.; Xevi, E. A GIS-based sensitivity analysis of multi-criteria weights. In Proceedings of the 18th World IMACS/MODSIM Congress, Cairns, Australia, 13–17 July 2009.
56. Dahal, R.K.; Hasegawa, S. Representative rainfall thresholds for landslides in the Nepal Himalaya. *Geomorphology* **2008**, *100*, 429–443. [CrossRef]
57. Pradhan, B. Landslide susceptibility mapping of a catchment area using frequency ratio, fuzzy logic and multivariate logistic regression approaches. *J. Indian Soc. Remote Sens.* **2010**, *38*, 301–320. [CrossRef]
58. Ding, N.; Melloni, L.; Tian, X.; Poeppel, D. Rule-based and word-level statistics-based processing of language: Insights from neuroscience. *Lang. Cogn. Neurosci.* **2017**, *32*, 570–575. [CrossRef]
59. Chung, C.J.F.; Fabbri, A.G. Probabilistic prediction models for landslide hazard mapping. *Photogramm. Eng. Remote Sens.* **1999**, *65*, 1389–1399.
60. Lee, S.; Pradhan, B. Landslide hazard mapping at Selangor, Malaysia using frequency ratio and logistic regression models. *Landslides* **2007**, *4*, 33–41. [CrossRef]
61. Sarkar, S.; Kanungo, D.P. An integrated approach for landslide susceptibility mapping using remote sensing and GIS. *Photogramm. Eng. Remote Sens.* **2004**, *70*, 617625. [CrossRef]
62. Van Westen, C.J.; Rengers, N.; Soeters, R. Use of geomorphological information in indirect landslide susceptibility assessment. *Nat. Hazards* **2003**, *30*, 399–419. [CrossRef]
63. Hashimoto, M. Plate tectonics and crustal deformation around the Japanese Islands. *J. Geophys. Res.* **1993**, *98*, 16149–16166. [CrossRef]
64. Müller, M.D.; Geiger, A.; Kahle, H.G.; Veis, G.; Billiris, H.; Paradissis, D.; Felekis, S. Velocity and deformation fields in the North Aegean domain, Greece, and implications for fault kinematics, derived from GPS data 1993–2009. *Tectonophysics* **2013**, *597*, 34–49. [CrossRef]

65. Wu, Y.; Li, L.; Chen, C.; Liang, H.; Guo, N.; Li, Y. GNSS deformation characteristics of North China in the past two decades. *Geod. Geodyn.* **2021**, *12*, 392–398. [CrossRef]
66. Lazos, I.; Papanikolaou, I.; Sboras, S.; Foumelis, M.; Pikridas, C. Geodetic Upper Crust Deformation Based on Primary GNSS and INSAR Data in the Strymon Basin, Northern Greece—Correlation with Active Faults. *Appl. Sci.* **2022**, *12*, 9391. [CrossRef]
67. Fuchs, G. On the geology of the Karnali and Dolpo regions, west Nepal. *Mitt. Geol. Ges. Wien* **1974**, *66*, 21–35.
68. Sharma, T.; Kansakar, D.R.; Kizaki, K. Geology and tectonics of the region between Kali Gandaki and Bheri Rivers in central west Nepal. *Bull. Coll. Sci. Univ. Ryukus* **1984**, *38*, 57–102.
69. Stöcklin, J. Geology of Nepal and its regional frame. *J. Geol. Soc.* **1980**, *137*, 1–34. [CrossRef]
70. DMG. *Geological Map of Karnali Province*; Department of mines and Geology: Kathmandu, Nepal, 2021.
71. Conforti, M.; Ietto, F. Modeling shallow landslide susceptibility and assessment of the relative importance of predisposing factors, through a GIS-based statistical analysis. *Geosciences* **2021**, *11*, 333. [CrossRef]
72. Dahal, R.K.; Hasegawa, S.; Nonomura, A.; Yamanaka, M.; Dhakal, S. DEM-based deterministic landslide hazard analysis in the Lesser Himalaya of Nepal. *Georisk* **2008**, *2*, 161–178. [CrossRef]
73. Bijukchhen, S.M.; Kayastha, P.; Dhital, M.R. A comparative evaluation of heuristic and bivariate statistical modelling for landslide susceptibility mappings in Ghurmi-Dhad Khola, east Nepal. *Arab. J. Geosci.* **2013**, *6*, 2727–2743. [CrossRef]
74. Akgun, A. A comparison of landslide susceptibility maps produced by logistic regression, multi-criteria decision, and likelihood ratio methods: A case study at Izmir, Turkey. *Landslides* **2012**, *9*, 93–106. [CrossRef]
75. Pradhan, B.; Youssef, A.M. Manifestation of remote sensing data and GIS on landslide hazard analysis using spatial-based statistical models. *Arab. J. Geosci.* **2010**, *3*, 319–326. [CrossRef]